Korean J. Chem. Eng., **29**(2), 154-161 (2012)
DOI: 10.1007/s11814-011-0166-6

Electrokinetic effects on fluid flow and particle transport

Myungman Kim†

Material Research Center, Samsung Advanced Institute of Technology (SAIT),
Samsung Electronics Co., Ltd., P. O. Box 111, Suwon 400-600, Korea
(*Received 18 April 2011 • accepted 28 June 2011*)

Abstract−The effect of counter-electroosmotic flow on the particle trajectories, the particle equilibrium position, and the critical flux was for the first time evaluated in normal flow filtration using numerical solution of the two-dimensional coupled Navier-Stokes, Nernst-Plank, and Poisson equations for a slit pore having a converging entrance. It was shown that the numerical results for the velocity profiles, ion concentrations, and induced streaming potential were in good agreement with analytical expressions obtained for a simple slit shaped. Numerical simulations for particle transport were performed at both constant pressure and constant filtration velocity in the presence of counter-electroosmosis. A significant shift in the particle trajectory and final equilibrium location were shown at constant pressure due to the reduction in the filtrate flux associated with the counter-electroosmotic flow arising from the induced streaming potential. However, simulations conducted at a constant filtration velocity showed only a very small effect of counter-electroosmosis, with the equilibrium position varying by less than 5% for calculations performed in the presence/absence of counter-electroosmosis. This result stems from a very small distortion in the velocity profile in the region above the pore due to the greater contribution from counter-electroosmosis in the region immediately adjacent to the pore wall. This paper will provide a useful framework to evaluate particle transport in the presence of electrokinetic phenomena.

Key words: Counter-electroosmosis, Electrostatic Interaction, Particle Trajectory, Normal Flow Filtration, CFD Simulations

INTRODUCTION

The membrane process, which has been widely using as a separation process in bioseparation, desalination and gas separation, now extends its application into energy harvest like fuel cell and lithium ion separation. Conventionally, membrane technology uses size difference between membrane pore and particle. It should be more than 10 in the ratio of size to get some feasible separation via membrane process. This size-based separation has some critical limitation, especially in protein separation since the size difference in protein particles is so small for membrane separation. To overcome the technical limitation, the additional driving force for protein separation was considered. That is electrostatic charge of protein particle and membrane surface by which one can separate two similar size proteins. This new concept of membrane separation causes one to develop many theoretical analyses of electrical phenomena in a membrane system focusing on electrostatic interactions between charged particles and the membrane. Furthermore, the fluid profiles can also be significantly affected by electrokinetic phenomena such as external electric field and induced electric field.

Most theoretical analyses of electrical phenomena in membrane systems have focused on electrostatic interactions between charged particles (or solutes/proteins) and the membrane. However, the fluid flow profiles can also be strongly affected by electrokinetic phenomena. Electrokinetic phenomena are directly associated with the motion of the fluid; e.g., the solvent flow that is generated by applying an external electric field (electroosmosis) or the induced electric field (or streaming potential) caused by the pressure-driven flow of an electrolyte solution through a charged membrane. The streaming potential also reduces the net rate of solvent flow through the membrane due to the effects of the electrical forces on the charged ions, a phenomenon known as counter-electroosmosis, since the solvent flow generated by the streaming potential is in the opposite direction of the pressure-driven flow. Electrokinetically driven solvent transport is of particular interest in microfluidic devices as a means to control the bulk flow of reactants and analytes [1-7].

Theoretical analyses of counter-electroosmosis [8] were initially developed for flow through charged circular cylinders with small surface potentials, i.e., under conditions where the classical Debye-Hückel approximation is valid. Anderson and Koh [9] extended these results to various non-circular cross-sections by numerically solving the non-linear Poisson-Boltzmann equation. The magnitude of the counter-electroosmotic flow was then evaluated by solving the Navier-Stokes equation including the electrical force terms. Saksena and Zydney [10] examined the effects of different pore size distributions on counter-electroosmosis through membranes consisting of a parallel array of cylindrical pores. In particular, calculations were performed to determine the effects of the pore size distribution on (1) the pressure-driven and electrically-driven solvent flow across the membrane, (2) the development of a streaming potential and its effect on the overall flux of the electrolyte solution, and (3) the evaluation of the membrane surface charge from experimental measurements of these electrokinetic phenomena. Bowen and Cao [11] examined the feasibility of using measurements of counter-electroosmosis to characterize the surface charge or surface potential of ultrafiltration/microfiltration membranes.

Although this approach was potentially attractive, more detailed analysis of the electrokinetic effects was needed to obtain any quantitative estimates of the membrane surface charge or potential.

†To whom correspondence should be addressed.
E-mail: myung1234@gmail.com

The objective of the studies performed in this paper was to evaluate the effects of counter-electroosmosis on the fluid flow profiles and particle trajectories in normal flow filtration. The first section of this paper focuses on evaluating the velocity profiles in a slit pore with a curved (converging) entrance and a diverging exit in response to an applied pressure (counter-electroosmosis). These velocity profiles are then used to evaluate the particle trajectories, with particular emphasis placed on determining the effects of counter-electroosmosis on the particle motion and transmission.

ANALYTICAL EXPRESSIONS FOR ELECTROKINETIC EFFECTS IN A SLIT

To verify the numerical formulation used to evaluate the electrokinetic flow, simulations were initially performed for a slit pore formed by two parallel plates, a simple geometry for which rigorous analytical solutions are available under conditions of low surface potential. The steady-state one-dimensional Navier-Stokes equations in a slit pore including the electrical stress term can be written as [12]:

$$\eta\frac{d^2v_y}{dx^2}+\rho_E E_y-\frac{dP}{dy}=0 \tag{1}$$

where v_y is the fluid velocity, η is the fluid viscosity, ρ_E is the local charge density, dP/dy is the pressure gradient, and E_y is the electric potential in lateral direction. The electric field (E_y) is equal to the gradient of the electrical potential, $-\Sigma\phi/\Sigma y$, where the electrical potential (ϕ) satisfies Poisson's equation:

$$\frac{\partial^2\phi}{\partial x^2}=-\frac{\rho_E}{\varepsilon_0\varepsilon_r}=-\frac{F}{\varepsilon_0\varepsilon_r}\sum_i z_i C_i \tag{2}$$

where x is the distance from the centerline of the pore, F is Faraday's constant, ε_0 is the permittivity of free space, ε_r is the dielectric constant of the medium, and z_i and C_i are the ion valance and concentration, respectively.

The velocity profile in a charged slit pore is evaluated by integrating Eq. (1) over the x-coordinate with ρ_E given by Eq. (2). A no slip boundary condition (v_y=0) is applied at x=x_p (the slit half-width) and symmetry conditions on the velocity and potential are applied at the pore centerline (x=0) yielding [12]:

$$v_y=E_y\frac{\varepsilon_0\varepsilon_r}{\eta}(\phi-\phi_{x=x_p})-\frac{dP}{dy}\frac{x_p^2-x^2}{2\eta} \tag{3}$$

The dependence of the electrical potential on the transverse (x) coordinate is determined by solving Eq. (2). The concentration of ion i is first evaluated by recognizing that there is no net ion flux in the x-direction:

$$N_i=D_i\frac{\partial C_i}{\partial x}+u_i z_i F E_x=0 \tag{4}$$

where $E_x=-\Sigma\phi/\Sigma x$, flow-induced electric potential and u_i is the mobility (=D_i/RT). Eq. (4) is integrated over the x-coordinate giving the ion (Boltzmann) distribution:

$$C_i=C_i^0\exp\left[-\frac{z_i F}{RT}(\phi-\phi_{x=0})\right]\approx C_i^0\left[1-\frac{z_i F}{RT}(\phi-\phi_{x=0})\right] \tag{5}$$

where the second expression is valid for low potentials (the Debye-Hückel approximation).

The electrical potential field is evaluated from Eq. (2) assuming a constant surface charge density on the pore boundary [12]:

$$\phi-\phi_{x=x_p}=\frac{q_p}{\varepsilon_0\varepsilon_r\kappa}\left[\frac{\cosh(\kappa x)-\cosh(\kappa x_p)}{\sinh(\kappa x_p)}\right] \tag{6}$$

where q_p is the surface charge density of the pore and κ^{-1} is the Debye length. Eq. (6) is substituted into Eq. (3) giving the following expression for the average velocity in the pore:

$$\langle V\rangle=\frac{x_p^2\Delta P}{3\eta\delta_m}-\frac{E_y q_p}{\kappa\eta}\left[\frac{\kappa x_p\cosh(\kappa x_p)-\sinh(\kappa x_p)}{\kappa x_p\sinh(\kappa x_p)}\right] \tag{7}$$

where δ_m is the membrane thickness. Eq. (7) can be used to directly evaluate the electroosmotic flow in a slit-shaped pore by setting ΔP= 0 and with E_y equal to the applied voltage divided by the membrane thickness.

In the absence of an externally applied electric field, the streaming potential (E_y) is evaluated using the constraint that there is no net electric current flow through the pore. The net current flow is equal to the sum of the convective and conductive contributions (the diffusive contribution is zero since the concentration gradients in the y-direction are assumed to be negligible):

$$I=\int_0^{x_p}v_y\rho_E dx+E_y\int_0^{x_p}c\,dx \tag{8}$$

where c is the local conductivity:

$$c=F^2\sum_i z_i^2 u_i C_i \tag{9}$$

The induced electric field (E_y) associated with the streaming potential is obtained by setting I equal to zero. Eqs. (2), (3) and (5) are substituted into Eq. (8) yielding:

$$E_y=\frac{\Delta P}{c_{eff}\delta_m}\frac{q_p}{\kappa\eta}\left[\frac{\kappa x_p\cosh(\kappa x_p)-\sinh(\kappa x_p)}{\kappa x_p\sinh(\kappa x_p)}\right] \tag{10}$$

with the effective conductivity (c_{eff}) in the pore given by

$$c_{eff}=c_{avg}+\frac{q_p^2}{4\eta}\left[\frac{\sinh(2\kappa x_p)-2\kappa x_p}{\kappa x_p\sinh^2(\kappa x_p)}\right] \tag{11}$$

The average velocity <V> can then be evaluated as

$$\langle V\rangle=\frac{x_p^2\Delta P}{3\eta\delta_m}-\left(\frac{\Delta P}{\delta_m c_{eff}}\right)\left(\frac{q_p}{\kappa\eta}\right)^2\left[\frac{\kappa x_p\cosh(\kappa x_p)-\sinh(\kappa x_p)}{\kappa x_p\sinh(\kappa x_p)}\right]^2 \tag{12}$$

The second term in Eq. (12) is the flow due to counter-electroosmosis and is proportional to the square of the surface charge density on the pore (under the conditions of low surface potentials where the Debye-Hückel approximation is valid).

THEORETICAL DEVELOPMENT

Although it is possible to develop analytical expressions for the ion concentrations, electrical potential and fluid velocity in a slit-shaped pore, the situation is much more complex in the region of converging flow near the entrance of the pore geometry examined previously elsewhere [13,14]. In particular, the system becomes truly two-dimensional, with the ion concentrations and electrical poten-

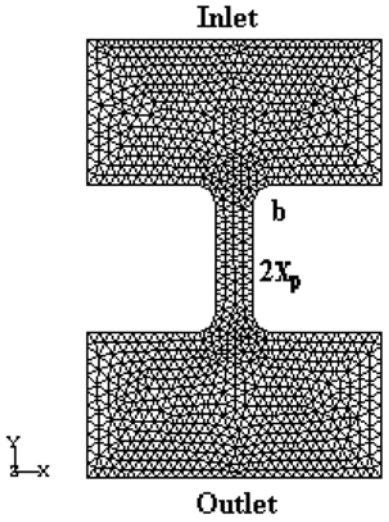

Fig. 1. Discretized system geometry.

tial now a complex function of both the x- and y-coordinates. This paper focuses on the fluid flow in normal flow filtration in which majority of flow entering the membrane pore has the velocity component both in x and y direction. That is the main reason why one can neglect the velocity component in z direction. In addition, the ion concentrations depend directly on the convective flow, thereby coupling the solution of the ion transport equation (the Nernst-Planck equation) with that of the momentum balance (the Navier-Stokes equation) and the electrostatic potential (Poisson's equation).

1. System Geometry

The geometry of the system of interest is shown in Fig. 1. This represents a single slit pore in a membrane, with the inlet and outlet regions formed by cylindrical (curved) surfaces to eliminate the mathematical discontinuity associated with a sharp boundary. The system is discretized with finite elements for numerical solution of the coupled equations. The width of the slit pore ($2x_p$) and the size of cylindrical edge that defines the pore entrance (b) can be adjusted to examine the effects of different pore geometries on the fluid flow and particle trajectories.

2. Boundary Conditions

Most analyses of electrokinetic phenomena assume either constant surface charge density or constant surface potential boundary conditions. These are really just two limiting cases describing the complex variation of the electrical charge/potential on the surface. If the pore has fixed charged groups, like the quaternary amine groups that are typically added to make membranes positively charged, then it is probably appropriate to assume that the charge on the membrane surface remains constant as one varies either the ion concentrations or the fluid flow. However, the charge on many polymeric membranes is determined at least in part by preferential ion adsorption or by the association/dissociation of various weak acidic or basic groups. In this case, it is likely that the surface charge will change as one varies the solution conditions, with the constant surface potential boundary condition potentially providing a more appropriate description of the underlying phenomenon.

To simplify the numerical analysis, model calculations were performed assuming a constant surface charge density:

$$\nabla\phi = -\frac{\sigma}{\varepsilon_0 \varepsilon_r} \tag{13}$$

which corresponds to a Neumann-type boundary condition. Constant surface charge conditions were applied at all solid surfaces (both inside and outside the pore). No-slip boundary conditions were applied for the fluid velocity, and no-flux boundary conditions were applied for the ion flux at all solid boundaries:

$$\mathbf{n}\cdot\mathbf{j}_i = 0 \tag{14}$$

where **n** is the unit normal to the membrane surface. Symmetry conditions for the fluid velocity, ion concentration, and electrical potential were applied at the pore centerline:

$$\frac{\partial v_y}{\partial x} = 0 \quad \frac{\partial c}{\partial x} = 0 \quad \frac{\partial \phi}{\partial x} = 0 \tag{15}$$

Inlet and outlet conditions correspond to uniform pressure, velocity, and ion concentrations.

In the case of counter-electroosmosis, the electrical potential was fixed (typically at zero) on the free surface at the inlet to the system. The condition of no net current flow was then applied at the exit (lower) surface. The local electrical current density is evaluated as

$$i_y = v_y \Sigma z_i e n_i - \sum_{i=1}^{n} D_i z_i e \frac{\partial n_i}{\partial y} + c\frac{\partial \phi}{\partial y} \tag{16}$$

where c, the electric conductivity of the fluid, is related to the local ionic concentrations as:

$$c = c_+ n_+ + c_- n_- \tag{17}$$

where c_+ and c_- are the electric conductivity of the cations and anions, respectively. In this paper, it is assumed that $c_+ = 5.01\times10^{-3}$ (Sm^2/mol) and $c = 7.63\times10^{-3}$ (Sm^2/mol) based on the values for Na^+ and Cl^- ions at 298 K [15].

The total current is evaluated by integrating Eq. (16) over the cross-sectional area:

$$I = \int_{x=0}^{x=x_i} \left[v_y \Sigma z_i e n_i - \sum_{i=1}^{n} D_i z_i e \frac{\partial n_i}{\partial y} + c\frac{\partial \phi}{\partial y} \right] dx \tag{18}$$

To apply no net current condition, simulations were performed with a guessed value of the electrical potential at the system exit ($y=y_2$), with the current evaluated from Eq. (18). New values of the exit potential were then selected, with the iteration continued until the total current was equal to zero (i.e., I=0). Eq. (18) was then used to evaluate the flow induced electric field (E_s) as:

$$E_s = \frac{\partial \phi}{\partial y} = \frac{\int_{x=0}^{x=x_i} \left[v_y \Sigma z_i e n_i - \sum_{i=1}^{n} D_i z_i e \frac{\partial n_i}{\partial y} \right] dx}{\int_{x=0}^{x=x_i} c\,dx} \tag{19}$$

RESULTS AND DISCUSSIONS

1. The Effect of Counter-electroosmosis

Typical velocity profiles accounting for the effects of counter-electroosmosis are shown in Fig. 2 at an applied pressure of ΔP=

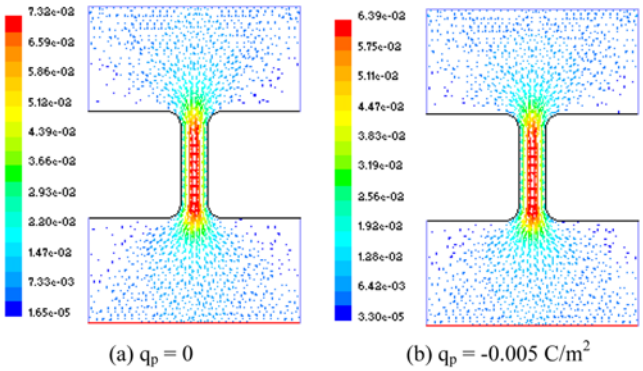

Fig. 2. Velocity profiles in the presence and absence of counter-electroosmosis for a pore with length=100 nm, x_p=12.5 nm, and b=12.5 nm.

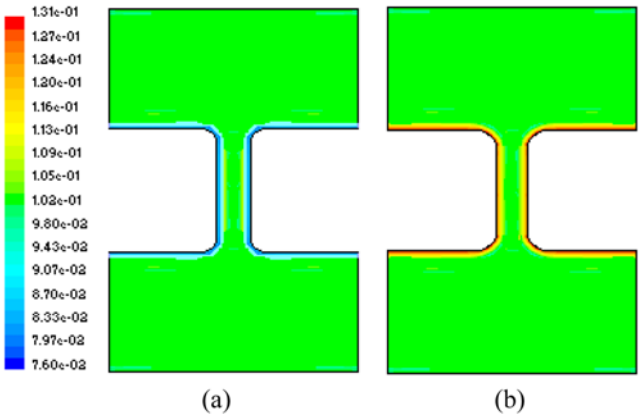

Fig. 4. Cation (a) and anion (b) concentration profiles.

10^5 N/m^2 for a membrane with a surface charge density of q_p=−0.005 C/m^2 (which is typical of a polyethersulfone membrane [16]), a pore length of 100 nm, a half-width of 12.5 nm, and b=12.5 nm. Calculations were performed at a solution ionic strength of 0.1 mol/*l* corresponding to a Debye length of 9.7 Å. The total volumetric flow rate through the pore was $Q=1.02\times10^{-9}$ m^3/s, compared to a value of $Q=1.28\times10^{-9}$ m^3/s for a neutral membrane under identical conditions, i.e., in the absence of counter-electroosmosis. The reduction in the flow-rate arises from the voltage driven flow associated with the induced streaming potential required to satisfy the electroneutrality (no current flow) condition across the membrane. The analytical results for Q and Q_0 were evaluated from Eq. (7) based on the total length of the pore giving $Q=\langle V\rangle A=8.61\times10^{-10}$ m^3/s and $Q_0=\langle V_0\rangle A=1.04\times10^{-9}$ m^3/s, corresponding to a ratio of Q/Q_0= 0.83 compared to Q/Q_o=0.80 for the numerical solution.

The small discrepancy between the numerical and analytical results arises from the converging/diverging entrance to the slit-shaped pores which reduce the effective length of the pore. This was confirmed by performing calculations for longer pores with smaller entrance radius (smaller values of b). For example, simulations for b= 8 nm and L=300 nm (a ratio of b/L=0.027 compared to b/L=0.125 for the simulations in Fig. 2 showed less than a 1% difference between the numerical and analytical results.

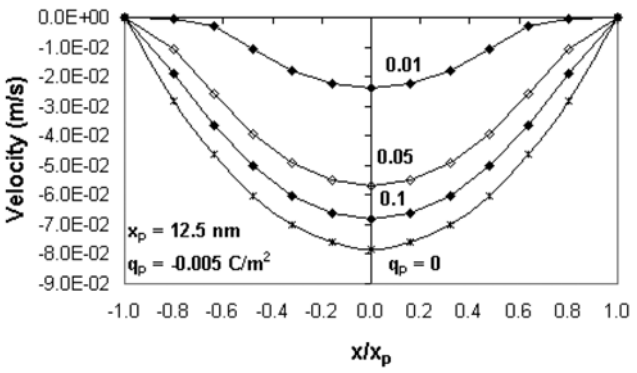

Fig. 3. Comparison between numerical results (symbols) and analytical solution (solid curves) for velocity profile accounting for counter-electroosmosis where the numbers on the curves represent ionic strength in units of mol/*l*.

The numerical results for the velocity profile within the pore, evaluated at the mid-point within the depth of the membrane, are compared with the analytical solution (Eq. (3)) in Fig. 3. Results are shown over a range of solution ionic strength. In each case, the numerical results are in excellent agreement with the analytical expression for the velocity profile, providing further validation of the numerical solution and the iterative approach used to evaluate the streaming potential and in turn the extent of counter-electroosmosis. The extent of counter-electroosmosis increases with decreasing ionic strength due to the increase in the double layer thickness and the corresponding increase in the magnitude of the streaming potential.

Contour plots showing the ion concentration profiles in the solution both inside and outside the pore are presented in Fig. 4. Results are shown for both the anions and cations at a bulk salt concentration of 0.1 M. There is steep change in the ion concentration near the entrance to the slit pore due to the electrostatic attraction of the positive cations and the electrostatic repulsion of the negative anions. The maximum anion concentration occurs deep within the pore and right at the surface of the membrane.

Fig. 5 presents a comparison of the numerical results with the analytical solution for the transverse ion concentration profiles within the pore, with the ion profiles evaluated analytically using Eq. (5)

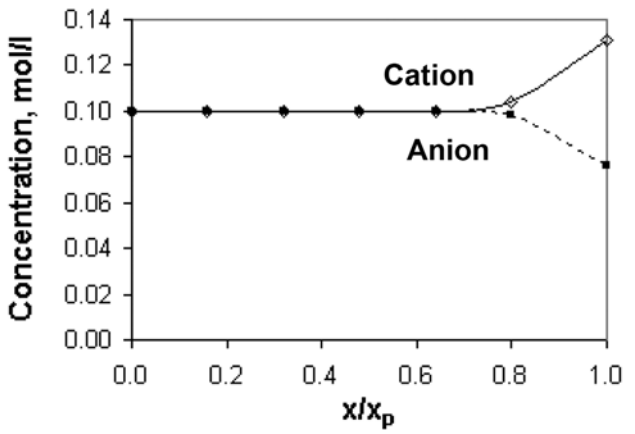

Fig. 5. Comparison of numerical (open symbols) and analytical (curves) results for the ion concentration profiles inside a slit pore at different axial positions during counter-electroosmosis.

where C_{i0} is the ion concentration at the pore axis (x=0). For the simulations with a 0.1 mol/*l* salt concentration, C_{i0} is equal to the bulk ion concentration since the electric double layer thickness (Debye length, κ^{-1}=9.74 Å) is much smaller than the pore size (r_0=12.5 nm). The numerical results for the cation and anion concentrations are in excellent agreement with the analytical values. The concentration of the cation near the pore wall is greater than that of the anion due to the electrostatic interactions, with the maximum cation concentration occurring at the surface of the negatively-charged pore wall.

Counter-electroosmosis refers to the "back flow" that is generated by the induced voltage (streaming potential) that arises during pressure-driven flow across a charged pore. The extent of counter-electroosmosis was evaluated iteratively, applying the constraint of electro-neutrality to converge on the value of the streaming potential that gives no net current flow through the membrane. A typical contour plot of the electrical potential is shown in Fig. 6. In this case, the condition of zero current flux is obtained with an electrical potential of V_{outlet}=−0.218 mV at the lower boundary of the system. The electrical potential is negative at the surface of the membrane due to the boundary condition of a constant negative surface charge density at the pore boundaries.

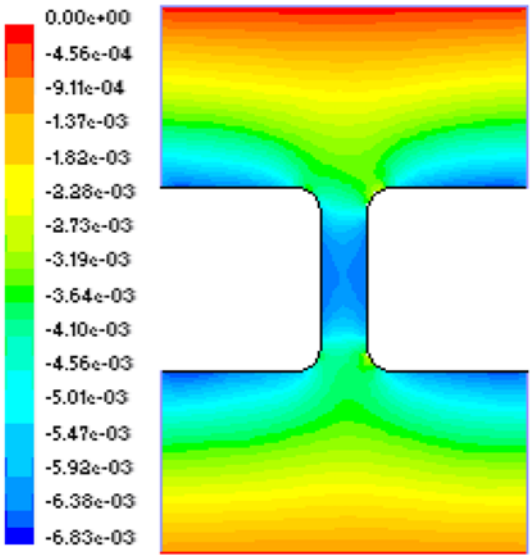

Fig. 6. Electrical potential profile for zero net current flow.

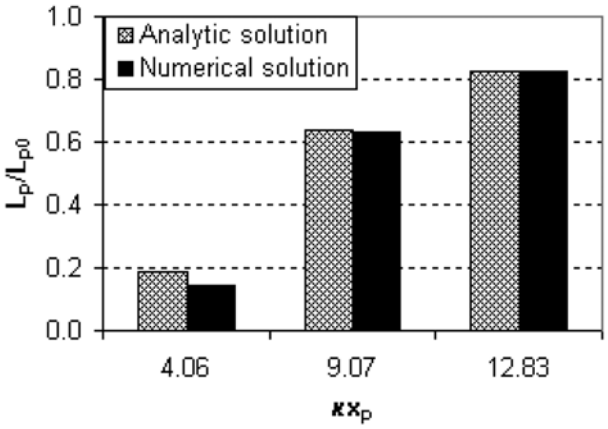

Fig. 7. The effect of counter-electroosmosis on the scaled permeability.

The reduction in the apparent hydraulic permeability of the membrane associated with the counter-electroosmotic flow is shown in Fig. 7 for several values of κx_p where κ^{-1} is the Debye length. Results are shown as the scaled permeability, L_p/L_{p0}, where L_{p0} is the hydraulic permeability evaluated in the absence of counter-electroosmosis, i.e., for a neutral membrane. The scaled permeability decreases with decreasing κx_p, varying from L_p/L_{p0}=0.82 at κx_p=12.8 to L_p/L_{p0}=0.63 at κx_p=9.1, and L_p/L_{p0}=0.14 at κx_p=4.1. This reduction in the scaled permeability is a direct result of the increase in counter-electroosmotic flow associated with the greater streaming potential in the low ionic strength solutions. The numerical results are in very good agreement with the analytical expressions at moderate and high ionic strength, with a somewhat greater discrepancy seen at κx_p=4.06. This discrepancy at low ionic strength is likely due at least in part due to the non-linear terms in the Poisson-Boltzmann equation, which are properly accounted for in the numerical solution but which are ignored in the analytical solution since Eq. (12) is developed using the Debye-Huckel approximation.

The effect of the pore size on the induced streaming potential gradient (E_s) is shown in Fig. 8, with the results plotted as the dimensionless streaming potential $\hat{E}_s=E_sL/(k_BT/e)$ where L is the total membrane thickness including the curved entrance and exit regions, e is the electronic charge, k_B is the Boltzmann constant, and T is the absolute temperature. The dimensionless streaming potential increases with increasing pore size, with the numerical results in good agreement with the analytical solution over the entire range of conditions. This increase in streaming potential with increasing pore size reflects the increase in the excess convective flux of the counter-ions which must be compensated for by an increase in electrokinetic flux associated with the streaming potential.

The effect of the size of the cylindrical pore opening (b) on the dimensionless streaming potential ($\hat{E}_s$) is shown in Fig. 9. $\hat{E}_s$ increases with increasing cylinder radius, but this effect is quite small with $\hat{E}_s$

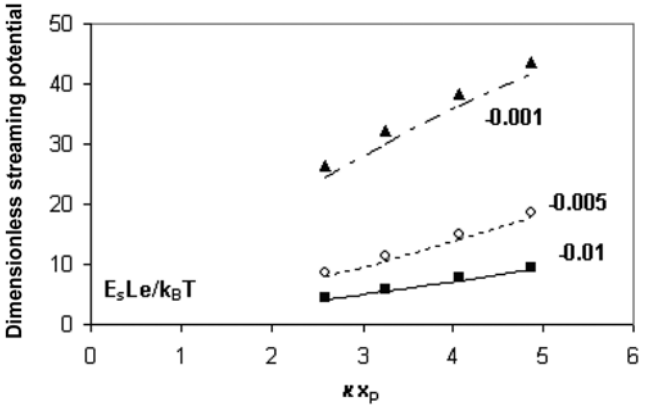

Fig. 8. Dimensionless streaming potential as a function of the dimensionless pore size at an ionic strength of 0.01 mol/*l*, b=12.5 nm, and $\Delta P=10^5$ N/m^2. The labels represent the membrane surface charge density in C/m^2. Curves and symbols are the analytical solution and numerical results, respectively.

varying from 14.6 at κb=4.9 to 15.1 at κb=2.6. The small increase in $\hat{A}_s$ with increasing values of b arises from the different effects of the detailed pore geometry on the flow profiles and electrical potential.

2. Particle Trajectory in the Presence of Counter-electroosmosis

To evaluate the effects of counter-electroosmosis on the particle trajectories, the results for the fluid velocity profiles accounting for counter-electroosmosis must be incorporated into the evaluation of the particle trajectories by integration of the Langevin equation as described in the previous publications [13,14]. The critical flux is defined as the permeate flux above which an irreversible deposit (fouling) appears. In the presence of electrostatic interaction between charged particle and charged membrane, the particle is able to enter the membrane pore when hydrodynamic force is greater than electrostatic repulsive force. In this paper, the critical flux was determined by particle trajectory, that is, the final location of a particle in the presence of electrostatic interaction, fluid dynamic and induced stream potential. However, the expression for the electrostatic force between the particle and the surface is strictly valid for interactions at constant surface potential, while the results for counter-electroosmotic flow were developed assuming that the membrane has a constant surface charge density. The surface potential of the particle was thus expressed in terms of the surface charge density (q) using the following expression:

$$\phi = \frac{aq}{\varepsilon_0 \varepsilon_r (1+\kappa a)} \tag{20}$$

The surface potential of the membrane was obtained directly from the numerical solution of the Poisson-Boltzmann equation as performed in the commercial software, FLUENT 6.0 (Lebanon, NH). As shown in Fig. 6, the membrane surface potential varies with position, with the maximum value of ζ=−6.25 mV obtained on the flat portion of the upper surface and in the space between the pore walls. This maximum value of the surface potential was used to evaluate the electrostatic interactions between the particle and the membrane following the approach described in elsewhere [13].

In the presence of counter-electroosmosis, the streaming potential will generate an electrophoretic transport of the particle associated with the induced electric field [16]. This electrophoretic transport

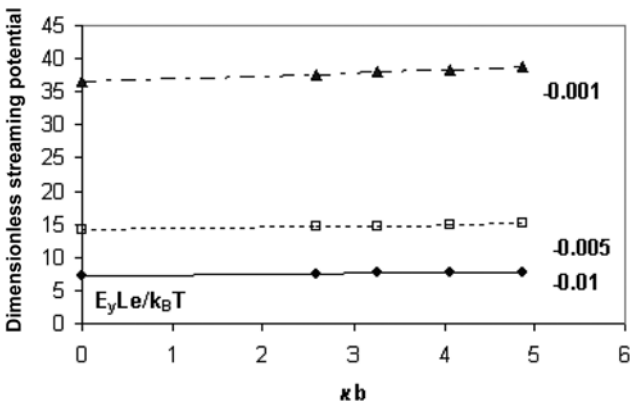

Fig. 9. The effect of the size of cylindrical edge (b) on $\hat{E}_s$ at various charge densities at an ionic strength of 0.01 mol/l and $\Delta P = 10^5$ N/m^2. The labels represent the membrane surface charge density in C/m^2. Curves and symbols are the analytical solution and numerical results, respectively.

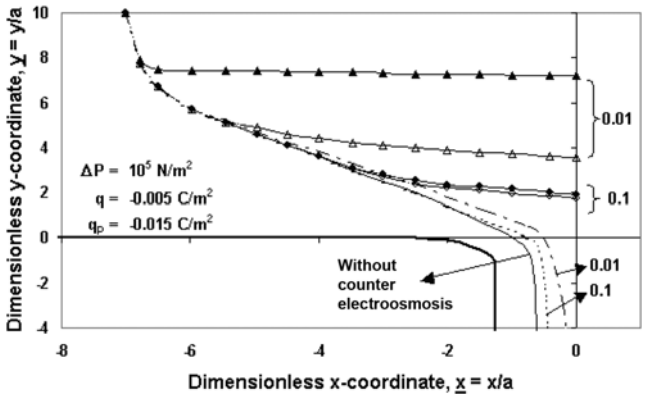

Fig. 10. Particle trajectories (curves with symbols) and fluid streamlines (curves without symbols) where filled and unfilled symbols represent particle trajectories with and without counter-electroosmosis. The numbers on the curves represent ionic strength in mol/l.

acts in the opposite direction of the convective flow. Previous work by Pujar and Zydney [16] showed that this electrophoretic transport was significantly smaller compared to the convective transport over a broad range of experimental conditions. Thus, no attempt was made to account for this electrophoretic particle flux in the evaluation of the particle trajectories. Fig. 10 shows the effects of counter-electroosmosis on the particle trajectories for simulations with $\Delta P = 10^5$ N/m^2, a=10 nm, and a particle charge of σ=−0.015 C/m^2 (corresponding to a particle surface potential of −6.25 mV). At an ionic strength of 0.1 M (corresponding to κx_p=12.8), the particle trajectory in the absence of counter-electroosmosis (discussed previously in elsewhere [13,14]) moves directly towards the pore axis, obtaining an equilibrium position at y=1.76, which corresponds to the location where there is no net force on the particle. The inclusion of counter-electroosmosis causes the particle trajectory to be shifted slightly upwards, with the particle becoming trapped at y=1.92. This increase in the height of the equilibrium location is a direct result of the reduction in the net fluid flow rate caused by the counter-electroosmotic backflow generated by the induced streaming potential, with the filtrate flux in the presence of counter-electroosmosis being 20% smaller than that through the neutral membrane.

The effect of counter-electroosmosis on the particle trajectories is much more pronounced at lower ionic strength (curves labeled 0.01 in Fig. 10) due to the greater electrical interactions at low salt concentrations. In this case, the equilibrium location shifts to y=7.19 in the 0.01 mol/l solution in the presence of counter-electroosmosis compared to y=3.58 in the absence of counter-electroosmosis. The simulations in Fig. 10 were performed at a constant applied pressure, which magnifies the effects of counter-electroosmosis. A corresponding set of simulations was conducted at a constant filtration velocity, with the calculations accounting for counter-electroosmosis performed by adjusting the applied pressure to keep the filtrate flux constant. Fig. 11 examines the equilibrium locations at both constant applied pressure ($\Delta P = 10^5$ N/m^2) and constant filtrate flux ($J = 6.46 \times 10^{-3}$ m/s), with the results normalized by y_{∞}, the equilibrium location in the absence of counter-electroosmosis. At high ionic strength (larger κx_p) there is relatively little effect of counter-electroosmosis, with similar results at both constant pressure and con-

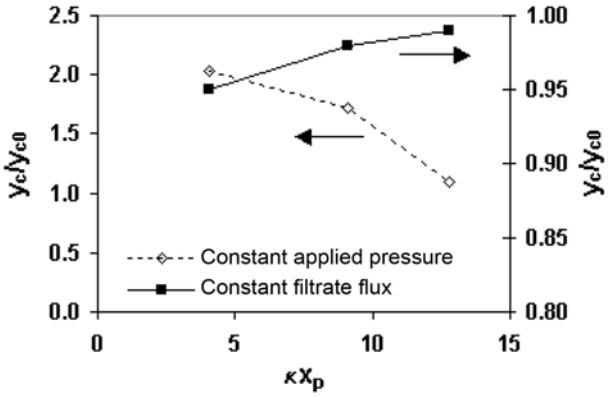

Fig. 11. Comparison of equilibrium locations at constant applied pressure and constant filtrate flux where x_p=12.5 nm and q_p=−0.005 C/m². y_{co} is the equilibrium location in the absence of counter-electroosmosis.

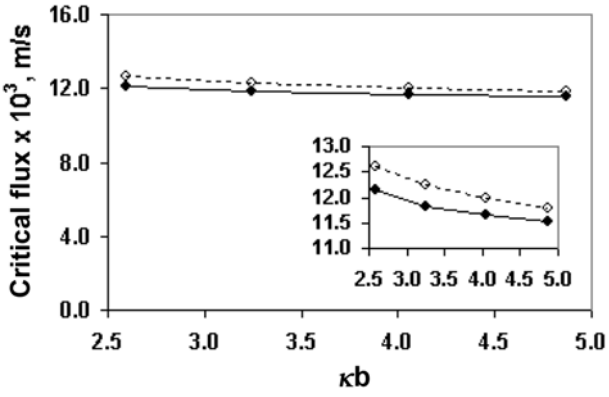

Fig. 13. The effect of the size of slit pore on the critical flux at an ionic strength of 0.01 mol/l, ΔP=10^5 N/m², x_p=12.5 nm, and q_p=−0.005 C/m² in the presence of counter-electroosmosis (dashed curve) and in the absence of counter-electroosmosis (solid curve).

stant flux. The effects of counter-electroosmosis become much more pronounced at low ionic strength, with the equilibrium position for simulations at constant pressure being a factor of 2 larger than those in the absence of counter-electroosmosis. The results at constant filtrate flux yield equilibrium positions in the presence of counter-electroosmosis that are within 5% of those determined in the absence of counter-electroosmosis, with the very small discrepancy arising from the distortion of the velocity profiles in the region above the membrane pore associated with the counter-electroosmotic flow.

The effect of counter-electroosmosis on the critical flux at different solution ionic strength is shown in Fig. 12. The critical flux decreases with increasing ionic strength (i.e., increasing κx_p) due to the increase in electrostatic shielding, a phenomenon that was discussed in much greater detail in elsewhere [13]. The effect of counter-electroosmosis becomes less pronounced at higher ionic strength (larger values of κx_p) due to the greater electrostatic shielding under these conditions.

The effect of the size of the slit pore on the magnitude of the critical flux at an ionic strength of 0.01 mol/l, ΔP=10^5 N/m², and q_p=−0.005 C/m² is shown in Fig. 13. The critical flux decreases with increasing pore size due to the reduction in the electrostatic repulsive force near the pore centerline for the larger pores. A similar effect is seen in the presence of counter-electroosmotic flow, with the critical flux being smaller due to the effects of counter-electroosmosis. This phenomenon is somewhat more pronounced in the smallest pores since the electrical double layer occupies a greater fraction of the pore under these conditions, although the magnitude of the effect remains less than 5% over the conditions examined in Fig. 13.

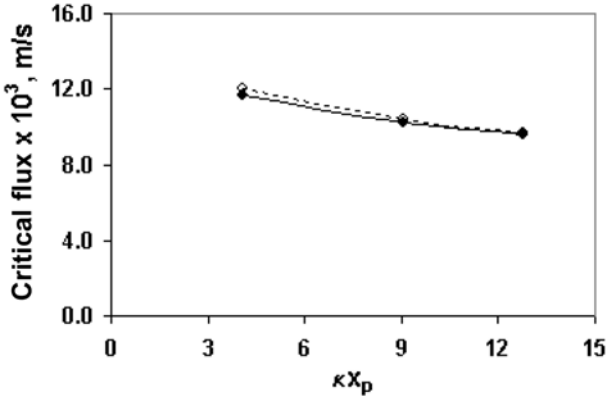

Fig. 12. Effect of ionic strength on the critical flux where b=12.5 nm and q_p=−0.005 C/m² both in the presence of counter-electroosmosis (dashed curve) and in the absence of counter-electroosmosis (solid curve).

CONCLUSIONS

Although there have been a number of theoretical studies of counter-electroosmosis in a variety of system geometries, the possible effects of this counter-electroosmotic flow on the particle trajectories in membrane filtration have not been evaluated previously. The results in this paper provide the first quantitative analysis of the role of counter-electroosmosis on the particle trajectories, the particle equilibrium position, and the critical flux in normal flow filtration. This was accomplished by first developing a framework to evaluate the fluid velocity profiles and electrostatic potential in a single pore system by numerical solution of the two-dimensional coupled Navier-Stokes, Nernst-Plank, and Poisson equations for a slit pore having a converging entrance. The numerical results for the velocity profiles, ion concentrations, and induced streaming potential are in good agreement with analytical expressions obtained for a simple slit shaped pore under conditions where entrance and exit effects are negligible. The presence of the cylindrical pore entrance only had a significant effect on the results for very short pores in which the entrance and exit regions occupy a significant fraction of the total pore length.

Simulations performed at constant pressure show a significant shift in the particle trajectory and final equilibrium location due to the reduction in the filtrate flux associated with the counter-electroosmotic flow arising from the induced streaming potential. In contrast, simulations conducted at a constant filtration velocity show only a very small effect of counter-electroosmosis, with the equilibrium position varying by less than 5% for calculations performed in the presence/absence of counter-electroosmosis. The small difference between the results at constant filtrate flux arises from a

very small distortion in the velocity profile in the region above the pore due to the greater contribution from counter-electroosmosis in the region immediately adjacent to the pore wall. Calculated values of the critical flux were nearly unaffected by the inclusion of counter-electroosmosis, demonstrating that the results reported elsewhere in this paper and in the literature (all of which have ignored the counter-electroosmotic flow) should provide an excellent description of the behavior of real membrane systems as long as the behavior is analyzed at a constant value of the filtrate flux, and not at the same applied pressure.

REFERENCES

1. A. Ajdari, *Phys. Rev. E*, **53**, 4996 (1996).
2. A. E. Herr, J. I. Molho, J. G. Santiago, M. G. Mungal, T. W. Kenny and M. G. Garguilo, *Anal. Chem.*, **72**, 1053 (2000).
3. S. Ghosal, *J.Fluid Mech.*, **459**, 103 (2002).
4. S. Yao, D. E. Hertzog, S. Zeng, J. C. Mikkelsen Jr. and J. G. Santiago, *J. Colloid Interface Sci.*, **268**, 143 (2003).
5. S. Yao and J. G. Santiago, *J. Colloid Interface Sci.*, **268**, 133 (2003).
6. C. M. Brotherton and R. H. Davis, *J. Colloid Interface Sci.*, **270**, 242 (2004).
7. D. Hlushkou, D. Kandhai and U. Tallarek, *Int. J. Numerical Methods in Fluids*, **46**, 507 (2004).
8. C. L. Rice and R. Whitehead, *J. Phys. Chem.*, **69**, 4017 (1965).
9. J. L. Anderson and W. H. Koh, *J. Colloid Interface Sci.*, **59**, 149 (1977).
10. S. Saksena and A. L. Zydney, *Biotechnol. Bioeng.*, **43**, 960 (1994).
11. W. R. Bowen and X. Cao, *J. Membr. Sci.*, **140**, 267 (1998).
12. J. S. Newman, Electrochemical systems. Englewood Cliffs, NJ, Prentice Hall (1991).
13. M.-M. Kim and A. L. Zydney, *J. Colloid Interface Sci.*, **269**, 425 (2004).
14. M.-M. Kim and A. L. Zydney, *Chem. Eng. Sci.*, **60** 4073 (2005).
15. R. F. Probstein, *Physicochemical Hydrodynamic An Introduction*, Stoneham, MA, Butterworth Publisher (1989).
16. N. S. Pujar and A. L. Zydney, *Ind. Eng. Chem. Res.*, **33**, 2473 (1994).